

UC Santa Cruz

UC Santa Cruz Previously Published Works

Title

Electrochemical Reactivity and Passivation of Silicon Thin-Film Electrodes in Organic Carbonate Electrolytes

Permalink

<https://escholarship.org/uc/item/2qn9j95v>

Journal

ACS Applied Materials & Interfaces, 12(36)

ISSN

1944-8244

Authors

Hasa, Ivana

Haregewoin, Atetegeb M

Zhang, Liang

et al.

Publication Date

2020-09-09

DOI

10.1021/acsami.0c09384

Peer reviewed

Carbonate Electrolytes

Ivana Hasa ^{[1]*#}, Atetegeb M. Haregewoin ^[1], Liang Zhang ^[2], Wan-Yu Tsai ^[3], Jinghua Guo ^[2],
Gabriel M. Veith ^[3], Philip N. Ross, ^[1] and Robert Kostecki ^{[1]*}

^[1] Energy Storage & Distributed Resources Division, Lawrence Berkeley National Laboratory, One Cyclotron Road, Berkeley, CA 94720, USA

^[2] Advanced Light Source, Lawrence Berkeley National Laboratory, One Cyclotron Road, Berkeley, CA 94720, USA

^[3] Chemical Sciences Division, Oak Ridge National Laboratory, Oak Ridge, Tennessee 37831, United States

Current address: WMG, The University of Warwick, Coventry CV4 7AL, United Kingdom.

*Corresponding author: ivana.hasa@warwick.ac.uk, r_kostecki@lbl.gov

Keywords

Lithium-ion battery, silicon anode, solid electrolyte interphase (SEI), interfacial reactivity, passivation, thin film, lithium ethylene decarbonate, SEI breathing.

Abstract

This work focuses on the mechanisms of interfacial processes at the surface of amorphous silicon thin-film electrodes in organic carbonate electrolytes to unveil the origins of the inherent non-passivating behavior of silicon anodes in Li-ion batteries. Attenuated total reflection Fourier-transform infrared spectroscopy (ATR-FTIR), X-ray absorption spectroscopy (XAS), and infrared near-field scanning optical microscopy (IR aNSOM) were used to investigate the formation, evolution and chemical composition of the surface layer formed on Si upon cycling. We found that the chemical composition and thickness of the solid/electrolyte interphase layer (SEI) continuously change during the charging/discharging cycles. This SEI layer “breathing” effect is directly related

1 to the formation of lithium ethylene dicarbonate (LiEDC) and LiPF_6 salt decomposition products
2 during silicon lithiation and their subsequent disappearance upon de-lithiation. The
3 detected appearance and disappearance of LiEDC and LiPF_6 decomposition compounds in the
4 SEI layer is directly linked with the observed interfacial instability and poor passivating behavior
5 of the silicon anode.
6
7
8
9

10 11 12 13 **1. Introduction**

14
15 High-energy lithium-ion batteries (LIBs) employing carbonate-based electrolytes
16 are thermodynamically unstable. The intrinsic limitations come from the reductive
17 decomposition of the electrolyte at the negative electrode, typically operating below the
18 electrochemical stability limit of the electrolyte.^{1,2} However, commercial LIBs can operate stably
19 due to the formation of the so called solid electrolyte interphase (SEI), which passivates the
20 surface of the anode and almost completely suppresses the electrolyte decomposition while
21 still allowing lithium ions transport.³⁻⁵ According to the common SEI layer functional model,
22 the solid electrolyte film acts as an interphase between the electrode and the liquid electrolyte
23 solution. The SEI model, proposed by E. Peled in 1979, is generally accepted today for all
24 alkali, alkaline earths metals and anode materials used in non-aqueous-battery systems.³
25
26
27
28
29
30
31
32
33
34
35
36
37

38 The SEI formation on a graphite electrode, which still represents the anode of choice for
39 LIBs, occurs mostly during the first cycle and it remains reasonably stable upon cycling,
40 ensuring relatively high (>99.9%) charge/discharge coulombic efficiency. Despite almost
41 5-10% of irreversible capacity loss associated with the SEI formation during the initial
42 charge-discharge cycles, a properly engineered graphite anode-based LIBs can provide excellent
43 energy density at adequate cycle and calendar life.^{6,7}
44
45
46
47
48
49
50
51
52
53
54
55
56
57
58
59
60

To increase energy density of LIBs, new type of non-carbonaceous anode materials have been proposed and studied as promising alternatives.⁸ Among them, lithium alloying anodes, and silicon in particular have attracted much interest because of their relatively low operating voltage and high theoretical gravimetric and volumetric capacity.^{9–12} Despite these encouraging parameters, alloying anodes present several challenges which still need to be addressed before a successful commercialization.¹³ The electrode failure mechanism is typically linked with a huge volume variation (280%) of silicon upon cycling.^{8,14,15} Such large volumetric changes induce a tremendous mechanical stress in the active material and results in particle cracking and mechanical disintegration of the composite Si electrode leading to gradual loss of electronic contact between Si particles and the electrode conductive matrix, electrode delamination from the Cu current collector and ultimately cell failure. These issues have been addressed successfully to some extent by smart active material and electrode design e.g., downsizing of Si particles, Si nano-architectures, advanced carbon matrixes and binders capable of containing the volumetric changes.^{14,16–19}

However, regardless of the mechanical degradation of the active material, the intrinsic instability of the SEI layer on silicon is the main challenge to be addressed for the successful implementation of the silicon anode in high performance LIBs.^{20–24} In fact, silicon exhibits a non-passivating behavior in the most commonly employed organic carbonate-based electrolytes. Contrary to graphite, Si anodes never fully passivate, with consequent continuous electrolyte decomposition^{20,25} responsible for charge/discharge coulombic inefficiency and rapid cell degradation during long-term cycling of Li-ion cells.²⁶ The unique electrochemical reactivity of silicon toward the electrolyte leads to large irreversible capacity loss, poor passivating behavior

with consequent gradual electrolyte consumption, lithium inventory shift in full cell

1 configuration and cell impedance increase due to surface film accumulation upon cycling.²⁷

2
3 A cyclic variation (breathing effect) of the SEI thickness has been observed upon
4 lithiation and de-lithiation, indicating the instability of this passivating layer and its continuous
5
6 change as a function of state of charge.²⁸
7
8
9

10 Veith et al.²⁹ revealed through neutron reflectometry that the breathing behavior of the
11 SEI is associated with a change in the chemistry of the compounds constituting the SEI.
12
13 Indeed, the SEI formation is strongly influenced by the electrolyte composition and the use of
14
15 additives.³⁰ By using an FEC-added electrolyte, the SEI thickens upon lithiation and becomes
16
17 more organic-like, while upon de-lithiation it becomes thinner and richer in inorganic
18
19 compounds.²⁴ Interestingly, the direction of the changes observed in thickness is the opposite
20
21 when using an FEC-free electrolyte.²⁴ Toney et al.³¹ detected through X-Ray reflectivity
22
23 measurements and high precision coulombic efficiency measurements that the SEI grows more
24
25 with increased time spent at low voltage value and that the growing rate is described by a
26
27 parabolic function.
28
29
30
31
32

33 On the other hand, the mechanism and kinetics of electrochemical reduction of the
34 electrolyte can be altered by the electrode surface structure and composition.^{32,33}
35

36 A fundamental understanding of electrochemical and chemical processes occurring at the
37
38 Si/electrolyte interface is essential for the development of the next generation of high-energy anode
39
40 materials.
41
42
43
44

45 Our approach toward that challenge consists of the use of model 50 nm amorphous thin-
46
47 film Si electrodes acting as standard platforms for the investigation of the interfacial properties.
48
49 Such Si model electrodes offer a consistent and well-defined electrode/electrolyte interface, which
50
51 is free of any possible interference from other passive and active components such as conductive
52
53
54
55
56
57
58
59
60

carbon additives and binders. Moreover, silicon thin-film electrodes with a thickness < 100 nm do not crack upon cycling³⁴ so, the intrinsic behavior of Si determines the electrochemical response of the electrode whereas the secondary degradation processes caused by the Si volume changes, cracking and fresh surface exposure are diminished.

2. Experimental

2.1. a-Si thin-film model electrode preparation

Amorphous silicon thin-film (a-Si-TF) electrodes were deposited by magnetron sputtering on a battery grade copper foil in an in-house (Oak Ridge National Laboratory) sputtering system. The Si thin-film were deposited for 5 minutes at 90 W power and 7.0 mtorr Ar pressure (99.9995%, Air Liquide), using a commercially available Si target (99.99% - Kurt J. Lesker) and a r.f. power supply. The silicon film was $50 \text{ nm} \pm 5 \text{ nm}$ thick with ca. 3 nm native SiO_2 layer and overall density of about 2.1 g cm^{-3} (based on neutron reflectometry measurements). The a-Si-TF samples were cut into disc electrodes of 12 mm diameter with ca. $1.2\text{-}1.3 \cdot 10^{-5}$ g of Si such that electrodes from the same vapor deposition were used throughout the experiments.

2.2. Electrochemical characterization

Three electrode Swagelok® T-type cells were assembled using glass fiber (Whatman GF/D) separator, and Li-foil reference and counter electrodes (Alfa Aesar), and filled with battery grade electrolyte, *i.e.* 1.2 M LiPF_6 in EC (ethylene carbonate): EMC (ethyl methyl carbonate) 3:7 wt.% (Tomiya Chemicals, Japan) in an argon filled glove box with a H_2O and O_2 content lower than 1 ppm (VAC Nexus one).

The cyclic voltammetry (CV) measurements were performed at a scan rate of 0.1 mV s^{-1} within the 0.05-1.5 V vs. Li^+/Li potential range. Cells were cycled galvanostatically at $5 \mu\text{A cm}^{-2}$,

which corresponds to $\sim C/10$ charge/discharge rate based on the theoretical capacity of the a-Si-TF electrodes ($\text{Li}_{4.4}\text{Si}$ fully lithiated phase). Electrochemical tests were recorded with a multi-channel potentiostat-galvanostat (VMP3, Biologic Science Instruments, France). All potentials are referred to the Li^+/Li reference electrode.

2.3. Surface analysis

Post-mortem analysis was performed on cycled electrodes recovered at different potential values during lithiation and de-lithiation. Electrodes were extracted from cycled cells inside an argon filled glove box and dried at room temperature. When specifically mentioned in the text, electrodes were rinsed with 200 μL of diethyl carbonate (DEC, anhydrous, $\geq 99\%$ Sigma Aldrich) for 10 seconds to remove residual electrolyte and dried at room temperature inside the glove box.

Ex situ attenuated total reflectance Fourier transform infrared (ATR-FTIR) spectroscopy measurements were performed inside an N_2 -filled environmental chamber (818GBB/Plaslabs). A Shimadzu IRTracer-100 spectrophotometer outfitted with the single reflection PIKE technologies MIRacle™ ATR sampling accessory equipped with Ge crystal was used to record ATR-FTIR spectra. The FTIR spectra were averaged over 200 scans with spectral resolution of 4 cm^{-1} .

For comparative purpose, the data were processed and analyzed using the Originlab software after proper baseline correction and normalization. To eliminate the electrolyte contribution in the spectra of the unwashed cycled electrodes, the subtractively normalized interfacial Fourier transform infrared spectroscopy (SNIFTIRS) method was used with a correct subtraction factor. Spectral subtraction has been performed between the “dried electrolyte” and the not washed cycled electrodes using the LiPF_6 absorption band at 780 cm^{-1} to determine the correct subtraction parameter. Indeed, despite LiPF_6 undergoes decomposition, it is assumed that a

1
2
3 consistent percentage of the salt (1.2M LiPF₆ solution) will be unchanged and its residual amount
4
5 in the dried electrolyte and the cycled electrode's surface will be reasonably comparable.
6

7
8 The topography measurement was conducted using a MFP3D atomic force microscope
9
10 (Asylum Research, Oxford Instrument Company, USA) with the non-contact mode. A Pt-Ir coated
11
12 AFM tip (BudgetSensors, ElectriMulti75-G) with a nominal spring constant of 3 N/m was used.
13

14
15 Near-edge X-ray absorption fine structure (NEXAFS) measurements were performed on
16
17 beamline 8.0.1 at the Advanced Light Source (ALS) in Lawrence Berkeley National Laboratory.
18
19 The NEXAFS spectra were recorded in total-electron-yield (TEY) mode by monitoring the sample
20
21 drain current. The energy resolution was set to 0.2 and 0.1 eV for the fluorine K-edge and Si L-
22
23 edge, respectively. Samples were prepared inside a glove box and transferred for analysis using an
24
25 in-house built airtight sample loader.
26
27

28
29 Near-field infrared imaging was conducted with a Neaspec NeaSNOM near-field imaging
30
31 system, using Pt-Ir coated AFM tips (NanoWorld, ARROW-NCPt), with a set of Daylight
32
33 Solutions quantum cascade tunable IR lasers (tuning range 1320-1420 cm⁻¹) as the excitation
34
35 source. Detection was performed with a liquid nitrogen-cooled HgCdTe photodetector (Kolmar
36
37 Technologies). The near-field IR setup was enclosed in a custom-built continuous-flow dry
38
39 nitrogen-purged glove box, allowing characterization of air- and water-sensitive compounds on
40
41 the sample surface.
42
43
44
45
46

47 **3. Result and discussion**

48
49 The electrochemical reduction of the electrolyte and SEI formation processes occurring
50
51 upon lithiation/de-lithiation of the a-Si-TF electrodes were first investigated by cyclic voltammetry
52
53 and galvanostatic charge-discharge tests.
54
55
56
57
58
59
60

1 The CV profile (Fig.1a) shows a small feature at 0.4 V, which is most likely related to an
2 early stage lithiation of silicon²³ or a partial reduction of the native oxide layer leading to
3 the formation of silicate species.^{35,36} At low potentials two main cathodic peaks associated with
4 the lithiation of amorphous silicon are observed at 0.2 V and 0.08 V. The two corresponding
5 de-lithiation peaks are observed during the anodic scan at 0.26 V and 0.48 V. The charge-
6 discharge efficiency of the lithiation/de-lithiation process has been calculated by integrating
7 the cathodic current at potentials <0.5 V vs. the total charge consumed during the
8 anodic scan. The charge/discharge efficiency of the 1st cycle was only ~78%. Upon further
9 cycling a more stable electrochemical behavior is observed characterized by a decrease of
10 the electrolyte reduction current, a reshaping of the lithiation peaks at potentials between
11 0.12-0.5 V and steady de-lithiation charge and current profile. While it is generally reported that
12 the magnitude of the cathodic and anodic charge for Si anodes increases upon cycling due to
13 particle cracking and electrochemical reactivity of freshly exposed silicon surface,^{23,37} this
14 behavior is not observed here due to the structural and mechanical integrity of the a-Si-TF
15 electrode.

16 During the first cathodic scan the onset of the cathodic current is observed at ca. 2.0 V,
17 which is generally ascribed to the early-stage formation of the SEI layer (Fig. 1b). The reduction
18 of the electrolyte cathodic peaks at 1.4 and 0.8 V are attributable to the decomposition of EMC
19 and EC, respectively. A non-negligible cathodic current contribution arises also from the copper
20 current collector through the pores of the Si thin film or the backside of the electrode. As reported
21 by El Kazzi *et al.*,³⁸ we confirm that the electrolyte reduction within the 2.0-0.5 V voltage range
22 is observed also by cycling the bare copper current collector. In fact, the corresponding cathodic
23 CV profiles of the Cu and a-Si-TF electrode, shown in Fig. 1b, overlap almost entirely at potential

1
2
3 > 0.3V with only a small extra current attributable to the first stage lithiation of silicon at 0.4 V.
4
5 Fig. 1c presents potential profiles of the first and second galvanostatic lithiation/de-lithiation
6
7 between 0.05 V- 1.5 V at 5 $\mu\text{A cm}^{-2}$. The potential profiles match well the CV plots i.e., all the
8
9 redox peaks observed at the CVs are also visible as plateaus in the galvanostatic curves and the
10
11 charge reversibility of the lithiation/de-lithiation process (77%) is also comparable.
12
13
14
15
16

17 3.1. Solvent decomposition species at the silicon/electrolyte interphase

18

19 The interfacial properties of the a-Si-TF model electrodes have been investigated by *ex situ*
20
21 ATR-FTIR spectroscopy at different potentials during the first lithiation/de-lithiation process.
22
23

24 **Figure 2**

25

26 Figure 2 (a-c) shows selected spectral regions of the ATR-FTIR spectra collected at 1.5 V,
27
28 0.5 V, 0.3 V, and 0.05 V during lithiation and at 1.0 V and 1.5 V during the following de-lithiation
29
30 process (see the green dots in Figure 1c). The electrodes have been analyzed as recovered from
31
32 cells i.e., without any rinsing process to remove residual electrolyte allowing residual EMC
33
34 evaporation. For the sake of reference, Fig. 2 displays the spectrum of the residual electrolyte on
35
36 a Cu-foil herein defined as “dried” electrolyte, which is a more representative reference spectra
37
38 for the ex-situ ATR-FTIR analysis performed on the recovered dried electrodes. The ATR-FTIR
39
40 reference spectra of the pristine liquid (“wet”), the “dried” electrolyte and EMC solvent are
41
42 reported in Fig. S1 in the Supplementary Information section. The main difference between the
43
44 spectra of the two electrolytes (“wet” vs “dried”) is related to the absence of the peaks associated
45
46 with the most volatile³⁹ solvent (EMC) indicated by green dotted lines.
47
48
49
50

51 The IR absorption peaks observed at 1.5, 0.5 and 0.3 V in Fig. 2 (a-c) belong to electrolyte
52
53 residue as shown in the spectrum of the dried electrolyte. However, close examination of the
54
55
56
57
58
59
60

1
2
3 spectrum of the a-Si-TF electrode in the fully lithiated state, *i.e.*, at 0.05 V reveals some notable
4 changes. Three new spectral features appear at 1652 cm⁻¹, 1460 cm⁻¹ and 1325 cm⁻¹, and
5 broadening of the electrolyte peaks at 1409 cm⁻¹, 1230 cm⁻¹, 1116 cm⁻¹ and 1060 cm⁻¹ is observed.
6
7 These new contributes are attributed to the presence of lithium ethylene dicarbonate (LiEDC,
8 (CH₂OCO₂Li)₂) on the electrode's surface ⁴⁰⁻⁴⁵. Table S1 in the Supplementary Information
9
10 section reports a comparative assignment of the peaks associated to the detection of LiEDC in the
11
12 present work with other reported studies.
13
14
15
16
17
18

19 The detection of LiEDC in the SEI layer does not represent itself a new finding. LiEDC
20 was firstly identified by Aurbach *et al.*^{46,47} as the primary decomposition product of EC containing
21 electrolytes on noble metals and lithium electrodes' surface. It has been reported that LiEDC is the
22 result of a single electron reduction process of EC according to the reaction Scheme 1⁴⁰:
23
24
25
26
27

28 **Scheme 1**

29
30 Later studies revealed the presence of LiEDC on nickel⁴⁰, carbonaceous⁴⁸ and silicon based
31 electrodes,²⁶ suggesting that LiEDC is the main component of the SEI film formed in EC-
32 containing electrolytes. However, Figure 2 (a-c) shows that LiEDC completely disappears from
33 the IR spectra during de-lithiation both at 1.0 V and 1.5 V. This behavior constitutes an important
34 observation that is directly related to the instability of the passive film on silicon electrodes during
35 cycling and the related charge/discharge coulombic inefficiency.
36
37
38
39
40
41
42
43

44 Interestingly, nothing other than the electrolyte and LiEDC IR absorption features are
45 observed in the three spectral regions at all potentials. This might be related to the lack of sufficient
46 FTIR sensitivity and selectivity, especially in the presence of large amount of the electrolyte
47 residue. To detect possible hidden components in the surface layer and evaluate the solubility of
48 the electrolyte decomposition products, two different approaches were undertaken. The first one
49
50
51
52
53
54
55
56
57
58
59
60

1
2
3 involved a rinsing step in DEC of the cycled electrodes (see experimental section), while the
4
5 second one consisted on the application of the a subtraction of the electrolyte peaks from the
6
7 experimental spectra obtained at different potentials (see experimental).
8
9

10 **Figure 3**

11
12 The ATR-FTIR spectra of the rinsed a-Si-TF electrode at different potentials are reported in Figure
13
14 3. The washing process leads to the disappearance of the electrolyte signal as well as other soluble
15
16 electrolyte decomposition products from the silicon surface, revealing the native SiO₂ layer at 1.5,
17
18 0.5 and 0.3V. A comparison of the FTIR spectra of the pristine uncycled electrode, the washed
19
20 electrode cycled up to 1.5 V and two reference spectra of amorphous SiO₂ is reported in Figure S2
21
22 in the Supplementary information section. It is shown that the spectral features between 1000 cm⁻¹
23
24 and 1300 cm⁻¹ can be indeed attributed to the Si-O vibrations of amorphous silicon oxide.
25
26
27

28 Figure 3 shows that the signal from SiO₂ tends to diminish and change its spectral shape as the
29
30 potential gets more negative, which suggests a participation of the oxide in the electrochemical
31
32 process as already previously proposed^{25,35,49,50}. The role of the oxide in the interfacial stability of
33
34 silicon electrode is still highly discussed and will be specific object of study of a following report.
35
36

37 Interestingly, the IR absorption features of LiEDC are still visible at 0.05 V as confirmed by the
38
39 IR absorption features at about 1651 cm⁻¹, 1402 cm⁻¹ and 1313 cm⁻¹ and 1089 cm⁻¹ (see Fig. 3 and
40
41 Table S1), indicating that LiEDC is not removed by rinsing the electrode in DEC.
42
43

44 Tasaky et al.⁵¹ has reported on the solubility of different lithium salts in organic solvents.
45
46 The molecular dynamic simulations demonstrated that the dissolution of organic salts is
47
48 exothermic as compared to endothermic dissolution of inorganic salts. Indeed, the enthalpy of
49
50 LiEDC dissolution in DMC (-21.65 kcal mol⁻¹) is negative with regard to positive values for
51
52 lithium oxalate (30.37 kcal mol⁻¹) or lithium carbonate (31.61 kcal mol⁻¹). The simulations were
53
54
55
56
57
58
59
60

1
2
3 in agreement with solubility values determined experimentally,⁵² indicating that LiEDC should be
4 readily soluble in organic polar solvents. However, LiEDC is still detected on the surface of the
5 lithiated electrode at 0.05 V even after a rinsing in DEC.
6
7

8
9
10 It is likely that EC decomposition and formation of LiEDC begins at higher potentials ca.
11 0.8 V. However, LiEDC is not observed at 0.5 V and 0.3 V, suggesting that LiEDC does not
12 precipitate on the electrode surface but instead dissolves in the electrolyte. The rate of formation
13 of LiEDC at lower potentials may increase to saturate the electrolyte and/or surface film and trigger
14 precipitation and agglomeration of LiEDC on the surface. Dissolution of LiEDC can involve
15 multiple steps, each with its own rate, and require a protracted amount of time to arrive at the
16 equilibrium. The parameters that can inhibit the dissolution of LiEDC in the electrolyte include
17 local viscosity of the solvents, surface tension, interfacial free energy, diffusion rate, and
18 adsorption to the lithiated silicon surface.²⁶
19
20
21
22
23
24
25
26
27
28
29

30
31 The electrode rinsing by organic carbonate solvents such as DEC to eliminate electrolyte
32 residue is often seen as a necessary step in *ex situ* studies of the film structure and composition.
33 On the other hand, the rinsing process may deeply affect and modify the film composition and
34 morphology, especially at high state of charge, when the electrode is more prone to react with the
35 rinsing agent to form products, which can also solubilize other film components.
36
37
38
39
40
41

42 To enable the detection of hidden compounds in the SEI layer, while avoiding the possible
43 side effects induced by the rinsing step, we adopted an alternative approach, consisting of
44 mathematical subtraction of the electrolyte reference spectrum from the experimental spectra
45 obtained at different potentials. Such an analysis is depicted in Fig. S3 in the Supplementary
46 Information section.
47
48
49
50
51
52
53
54
55
56
57
58
59
60

Again, new spectral features appear only at the FTIR spectra of the fully lithiated sample (0.05 V) at 1654 cm^{-1} , 1326 cm^{-1} , 1110 cm^{-1} and 1062 cm^{-1} , which are attributed to LiEDC. Some additional peaks that appear at ca. 800-900 cm^{-1} can be attributed either to LiEDC, polyethylene glycol, P-F and/or P-O-F containing compounds.

Interestingly, Ross et al.⁴⁸ reported on the evolution of the passivation film formed on graphite electrodes by using the same electrolyte employed in this work. FTIR analysis revealed that the main decomposition products of EC on the external surface of graphite are polyethers like polyethylene glycol (PEG) species (also known as polyethylene oxide (PEO)) and lithium oxalate.⁴⁸ Indeed, it is proposed that lithium oxalate, together with lithium ethane-1,2-bis(olate), is formed through a secondary two electron reduction process (see Scheme 2) occurring at the expenses of LiEDC, which in turn is formed as a decomposition product of EC.⁴⁸

Scheme 2

To highlight possible differences between the SEI products observed on graphite with those formed on the silicon thin films herein studied, FTIR analysis on reference compounds has been performed and compared with the spectra of the cycled a-Si-TF electrode. Figure 4 shows *ex situ* FTIR spectrum of the rinsed a-Si-TF electrode lithiated at 0.05 V, and reference spectra of LiEDC,⁴⁰ polyethylene glycol (PEG), lithium oxalate, lithium carbonate and lithium ethoxide.

Figure 4

In fact, the FTIR spectrum of the a-Si-TF electrode at 0.05 V may appear as a superposition of the main peaks of lithium oxalate (1654 cm^{-1} , 1327 cm^{-1}) and polyethylene glycol (1050 cm^{-1} -1150 cm^{-1}) but the dominant spectral features of the a-Si-TF electrode match those of LiEDC much better than lithium oxalate. As a matter of fact, the spectral feature at ~1402 cm^{-1} observed for the cycled electrode is not observed for lithium oxalate as well as the broad peaks centered at ~1100

cm⁻¹ and 830 cm⁻¹, which can be associated instead to LiEDC (see also peak assignment for LiEDC in Table S1) and a merged contribute arising from oligomeric polyethylene glycol species.

It is worth mentioning that other alkyl carbonates can be formed upon solvents decomposition such as dilithium butylene dicarbonate (Li₂BDC), LiO(CH₂)₂CO₂(CH₂)₂OCO₂Li and Li(CH₂)₂OCO₂Li, which have been recently detected by solid-state NMR.⁵³ Given the similar functional groups and the lack of reliable reference compounds, the assignment of the peaks to the mentioned chemical species is rather difficult, thus we cannot completely exclude their presence on the silicon surface. It is believed that for EC reduction, Li₂CO₃ is likely to form at low concentration of EC, while LiEDC is more likely to form at high concentration, highlighting the importance of the kinetic barriers of these reactions compared to thermodynamics.⁶

From the results reported in Fig. 4, the presence of Li₂CO₃ can also be excluded since the main characteristic spectral features are not observed in the spectrum of the washed electrode.

Overall, from the comparison of the FTIR spectrum with those of the available reference compounds, the formation of lithium oxalate and lithium carbonate can be excluded, indicating LiEDC as the final single electron reduction product of EC with additional contributes arising from polyethylene glycol-like oligomeric as reported by Nanda et al.⁵⁴ Compared to previously reported data on graphite electrodes,⁴⁸ this is a clear distinction between the passivation film formed on graphite and silicon-based anodes in EC containing electrolytes. In addition, it should be noted that the chemical species observed after decomposition of LiEDC on graphite are clearly present both in lithiation and after de-lithiation, highlighting a remarkable difference between the stability of the passivation layer formed on graphite and silicon, with the latter one being more unstable.

To gain more insight in to LiEDC distribution in the surface layer on the lithiated a-Si-TF electrode, apertureless near-field IR scanning optical microscopy (IR aNSOM) imaging has been

carried out. IR aNSOM uses a metallized AFM tip in contact with the sample surface as an optical probe for nanometer-resolution IR spectroscopy and imaging measurements.⁵⁵ The AFM tip is illuminated by a focused IR light beam, which produces a strong electromagnetic field at the tip apex due to the lightning rod effect.⁵⁶ Image contrast in IR aNSOM is obtained by the relative local absorption of chemical compounds present at the tip location as it is raster-scanned along the surface. IR aNSOM is one of few optical methods, which can provide subwavelength resolution of the functional composition and structure of the SEI layer. The ability of IR aNSOM to identify the SEI's chemical constituents at their natural length scale has already been successfully demonstrated for model highly oriented pyrolytic graphite (HOPG) and Sn electrodes.^{57,58}

Figure 5

Figure 5 depicts IR aNSOM $1\ \mu\text{m} \times 1\ \mu\text{m}$ images collected at 1360 , 1330 , and $1410\ \text{cm}^{-1}$ for the lithiated a-Si-TF electrode at $0.05\ \text{V}$. The AFM topography map of the surface film shows a complex surface morphology with particles of various sizes, agglomeration, distribution and roughness. For comparative purpose, the AFM images of the copper current collector and the uncycled pristine a-Si-TF are reported in the Figure S4 (Supplementary Information section). The observed variation in chemical contrast as a function of IR wavelength, indicates significant variation in surface structure and chemical composition. The images at 1330 and $1410\ \text{cm}^{-1}$ excitation wavelength (Fig. 5c, 5d), which correspond to the $\nu_{\text{C=O}}$ and $\delta_{\text{C-H}}$ absorption bands of LiEDC, respectively, show strong absorption of two large agglomerates sitting on top of a non-absorbing, densely packed inner layer. Interestingly, the IR aNSOM image at $1360\ \text{cm}^{-1}$ revealed no significant absorbance at any location on the surface. The IR absorbing behavior of the large aggregates at 1330 and $1410\ \text{cm}^{-1}$ match FTIR spectral characteristics of LiEDC and indicate random distribution of LiEDC particles on the electrode surface.

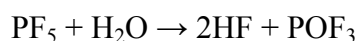
3.2. Salt decomposition species at the silicon/electrolyte interphase

Ex situ ATR-FTIR spectra of the unwashed and washed a-Si-TFs electrodes in the 1000-700 cm⁻¹ spectral region are reported in Figure 6.

Figure 6

The spectra recorded at different potentials clearly indicate accumulation of LiPF₆ decomposition compounds.⁵⁹ The sharp peak observed at ~ 840 cm⁻¹ for the sample scanned to 1.5 V (Fig. 6a) is associated with the P-F vibrations in PF₆⁻ from the salt residue. This peak progressively broadens and increases in intensity from side-bands contributions at 887, 810 and 745 cm⁻¹ during cathodic scan to reach maximum at 0.05 V. Similarly to LiEDC spectral behavior, this broad maximum decreases significantly upon de-lithiation.

LiPF₆ can precipitate and dissociate at the electrode's surface to give rise to secondary reactions with trace amounts of H₂O in the electrolyte to give rise to F-, -P-F and -P-O-F IR bands from LiPF₆ decomposition compounds according to the reaction scheme:⁶⁰⁻⁶²

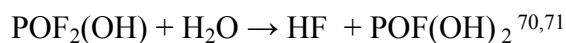
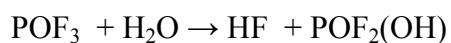
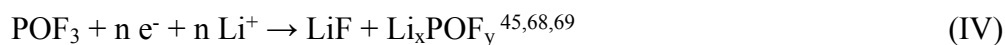


The HF generated by LiPF₆ hydrolysis^{61,63,64} can attack the thin native SiO₂ passivating layer typically covering the silicon surface leading to the formation of SiO_xF_y.^{38,63} It has been proposed that the etching of SiO₂ by HF evolves through four steps, each of them based on a coordinated attack of the Si-O bond by an HF molecule generating a Si-F bond. Further theoretical calculations indicate that the reaction path may consist of a coordinated attack of the Si-O bond by H⁺ and

HF_2^- .⁶⁵ The Si-F vibrations can be typically detected at ca. 930 cm^{-1} e.g., SiO_xF_y exhibits an IR band near 936 cm^{-1} from SiF_2 units.^{66,67}

Ex situ FTIR spectra of the unwashed a-Si-TF sample (Fig. 6a) show no trace of IR bands in this region. However, for the washed electrodes (Fig. 6b) a small maximum at slightly higher frequencies appears at 0.3 V and turns into a distinct peak at 0.05 V to disappear upon de-lithiation. So, we may reasonably assume that the native SiO_2 layer is reactive toward the electrolyte. Indeed, the feature attributed to the Si-O vibrations undergoes changes as indicated by the reshaping of the peaks with increasing negative potential. Interestingly, these features are not completely recovered after de-lithiation at 1.5 V, further suggesting irreversible reaction(s) of the native SiO_2 layer (Fig. 6b) most likely converted to silicate species as previously reported.^{25,38,63}

The POF_3 species formed upon reduction of LiPF_6 can react further with trace amounts of H_2O according to the reaction scheme:



It has been reported that the precipitation on the anode's surface of solid products such as LiF , POF_3 , $\text{POF}_2(\text{OH})$, and $\text{POF}(\text{OH})_2$ as constituents of SEI layer, leads to increased cell impedance in view of their ionically and electronically insulating nature.^{70,71} The F:P atomic ratio in the SEI layer is generally higher than the otherwise expected 6:1 for LiPF_6 .⁴⁴ This is most likely explained by considering the formation of soluble P containing species such as $\text{F}_2\text{PO}_2\text{Li}$,

phosphates and fluorophosphates, *i.e.* OP(OCH₃)₃, OPF(OCH₃)₂, and OPF₂(OCH₃) as previously detected in solution by nuclear magnetic resonance (NMR) spectroscopy and gas chromatography with mass selective detection (GC-MS) by Lucht et al.⁴⁴ All the above-mentioned species containing P-F and P-O-F bonds can be associated with the IR peaks observed within the 800-900

cm⁻¹ spectral region. Interestingly, after washing the a-Si-TF electrodes, most of those features disappear and only contributions from the native SiO₂ film are detected at 1.5 and 0.5 V. This suggest that the majority of the formed compounds are easily soluble in organic carbonate solvents, except for a small fraction, which is tightly bonded to the lithiated silicon surface, as observed for the electrode cycled at 0.05 V. A P-O-F containing compounds can be formed upon chemical reaction of Li₂CO₃ with LiPF₆ according to the scheme:



However, we were unable to detect Li₂CO₃ on the passive layer of the a-Si-TF electrodes. Similarly, it has been proposed that also LiEDC can react with LiPF₆ with the consequent formation of oligo-ethylene oxide substituted phosphates, such as F₂PO₃Li (soluble) and oligoethylene oxide ethers.⁴⁴

In all the reactions schemes mentioned above LiF appears to be an omnipresent byproduct. LiF is IR active at frequencies below 600 cm⁻¹, which is beyond the spectral region limits dictated by the ATR-FTIR instrument used. Thus, to detect LiF presence in the passive layer on Si, *ex situ* F K-edge TEY XAS analysis was performed (Fig. 7).

Figure 7

As expected, F⁻ containing compounds are not detected for the pristine a-Si-TF electrode. However, when the electrode is scanned to 1.5 V, the spectrum starts showing a broad feature that resembles the spectrum of LiPF₆. Interestingly, at more cathodic electrode potentials <0.5 V the

XAS spectra matches the reference spectra of LiF, which is still present on the electrode's surface at the end of the anodic scan.⁷²

It appears that LiF, contrary to soluble P-O-F and P-F species, forms early on the silicon surface and it stays there permanently. The effect of LiF on the SEI stability is not the subject of this work, however since LiF is a poor Li ionic conductor, the continuous formation of large amounts of LiF is expected to lead to an increased cell impedance. However, its functionality might also depend on its morphology and distribution in the film.^{43,73} On the other hand, LiF is also a poor electronic conductor that can hinder further charge transfer across the interface and inhibit the electrolyte decomposition.

3.3. The "breathing effect" of the silicon/electrolyte interphase

The peculiar behavior of the carbon-, fluorine- and phosphorus-containing species in the surface film during cycling suggest a gradual reformation of the passive layer during the first charge/discharge cycle. Figure 8 shows *ex situ* Si L-edge XAS TEY spectra of the SEI layer at the washed a-Si-TF electrode formed during the 1st cycle at different potentials.

Figure 8

Due to the shallow detection depth (about 5 nm), the double feature of SiO₂ detected between 106-109 eV energy range, gradually decreases in intensity and finally disappears in the lithiated state at 0.05 V, suggesting the formation and thickening of the SEI layer which hinders the signal from the SiO₂ underneath. Upon de-lithiation, the SiO₂ feature reappears again indicating a considerable reduction of the SEI layer thickness. The XAS results confirm the dynamic behavior of the SEI layer during cycling induced by the appearance and disappearance of LiEDC and P-F and P-O-F-containing compounds.

To evaluate the impact of this behavior of the electrochemical performance of the a-Si-TFs electrode we extended our investigations into the second galvanostatic charge-discharge cycle. *Ex situ* ATR FTIR spectra of the a-Si-TFs electrode at 0.05 and 1.5 V during 1st and 2nd galvanostatic cycles are shown in Figure 9.

Figure 9

Consistently, the peaks associated with the formation of LiEDC appear at 0.05 V and disappear during the following de-lithiation at the end of the first and second cycle. A similar trend is observed for the P-O-F and P-F containing compounds observed at lower frequencies and for the oligomeric polyethylene glycol species (see also reference spectra PEG species in Fig. 4) as indicated by the broad peaks at 1000-1100 cm^{-1} observed only in discharge. The peak centered at ca. 850 cm^{-1} constantly broadens and shrinks upon charging and discharging, respectively. However, contrary to the behavior of LiEDC, intensity of these low frequency bands tends to increase with cycling suggesting a non-complete dissolution during the first de-lithiation and gradual accumulation during cycling.

This constant reformation of the SEI layer has been previously observed and it is commonly referred as the “breathing effect”.^{24,28,29,74}

LiEDC, polyethylene glycol oligomers, LiF and P-F and P-O-F containing compounds detected in the surface film at the lithiated Si disappear partially or completely during de-lithiation, except for LiF, which remains intact. There is no evidence of electrochemical oxidation of these species during the anodic scan. Thus, this behavior can only be explained by a slow dissolution of these species in the electrolyte, which to some extent may be associated with the mechanical detachment from the surface of the electrode.

Dissolution rate generally refers to a kinetic process and expresses the net rate of reaction with respect to the final equilibrium state described by solubility.⁷⁵ A solute can be very soluble but still require a considerable amount of time to dissolve in the solvent, and conversely, a solute may have poor solubility in a solvent, yet its dissolution rate can be fast.⁷⁶ The dissolution process is closely linked with disintegration, deaggregation and dissolution itself and each of these steps occurs at its own rate. On the other hand, intermolecular interactions between solute particles and solvents mixture depends on the available effective interfacial contact area and local interfacial energetics.⁷⁶ Therefore the observed differences in the rate of dissolution of LiEDC, organic and inorganic compounds in the SEI layer on Si may be associated with the constantly shifting chemical equilibria between the solid residues in the film, and soluble and likely viscous electrolyte decomposition products, which are constantly replenished at low potentials but eventually dissipate slowly in the electrolyte at higher potentials. Finally, various diffusion rates of different molecules into the electrolyte bulk can alter the dissolution process of the film. This also explains why rinsing tend to remove some compounds faster whereas it has a little or no effect on other SEI layer constituents. This effect can be amplified by the varying affinity of LiEDC and other compounds to Li_xSi surface as composition of the electrode varies during cycling.²⁶

4. Conclusions

The results of this study indicate a dynamic growth and dissolution of the SEI layer on silicon during lithiation/de-lithiation, respectively. The SEI layer “breathing effect” is directly related to the formation of LiEDC (solvent decomposition product) and P-F and P-O-F containing compounds (salt decomposition products) and their disappearance upon de-lithiation. The observed “breathing effect” of the SEI layer on silicon is a clear manifestation of the intrinsic

interfacial instability and poor passivating behavior of the silicon anode in organic carbonate electrolyte and is explained by considering a slow dissolution of the species in the electrolyte. LiPF_6 decomposition products including P-O-F and P-F containing compounds undergo a non-complete dissolution during the first de-lithiation suggesting an accumulation of these species on the electrode's surface. LiF instead, forms early on the silicon surface and it stays there permanently, representing a stable component of the SEI layer.

LiEDC is a soluble salt in carbonate solvents, and its formation from EC decomposition begins at ca. 0.8 V. However, LiEDC is not observed until 0.05 V, suggesting that LiEDC does not precipitate on the electrode surface but instead dissolves in the electrolyte. The rate of formation of LiEDC at lower potentials increases to saturate the electrolyte and/or surface film and trigger precipitation and agglomeration of LiEDC on the surface. This effect is amplified by the affinity of LiEDC and other compounds to the Li_xSi surface as the composition of the electrode changes upon cycling. The disappearance of LiEDC upon de-lithiation can be explained considering LiEDC deaggregation from the lithiated silicon surface by the removal of lithium from silicon and consequent solubilization back into the electrolyte.

The origin of this phenomenon is linked directly with the overall composition and/or morphology of the film and its interactions with the Li_xSi electrode and the electrolyte, which appear to be strongly dependent on the electrode potential.

The precise identification of chemical species, their exact distribution and function in the electrode and electrolyte interphase with regard to its passivating properties still remains as the key barrier for the development of practical silicon-based anodes for high-energy Li-ion cells, highlighting the importance of further studies in this direction.

Associated Content

Supporting Information

Comparison of the ATR-FTIR spectra of Generation 2 electrolyte (1.2M LiPF₆ in EC:EMC 3:7 wt.%) in standard condition (“wet”) and after evaporation of EMC (“dried”) compared with EMC solvent. Assignment of the peaks observed for LiEDC in this work and other published results. ATR-FTIR spectra of pristine a-Si-TF and SiO₂ reference compounds. ATR-FTIR spectra obtained by subtracting the reference spectra of the “dried” electrolyte to all the spectra of the cycled electrodes. AFM topography of the copper current collector and pristine uncycled a-Si-TF.

Acknowledgements

This work was supported by the Assistant Secretary for Energy Efficiency and Renewable Energy, Office of Vehicle Technologies of the U.S. Department of Energy under Contract No. DE-AC02-05CH11231, under the Silicon Electrolyte Interface Stabilization (SEISta) Consortium directed by Brian Cunningham and managed by Anthony Burrell. The XAS measurements were performed at the Advanced Light Source in Lawrence Berkeley National Laboratory, supported by DOE under Contract No. DE-AC02-05CH11231. A portion of this work (GMV – film growth) was performed at the Oak Ridge National Laboratory, which is managed by UT Battelle, LLC, for the U.S. Department of Energy (DOE) under contract DE-AC05-00OR22725.

References

- (1) Scrosati, B.; Garche, J. Lithium Batteries: Status, Prospects and Future. *J. Power Sources* **2010**, *195* (9), 2419–2430.
- (2) Goodenough, J. B.; Park, K. S. The Li-Ion Rechargeable Battery: A Perspective. *J. Am. Chem. Soc.* **2013**, *135* (4), 1167–1176.

- 1
2
3 (3) Peled, E. The Electrochemical Behavior of Alkali and Alkaline Earth Metals in Nonaqueous
4 Battery Systems—The Solid Electrolyte Interphase Model. *J. Electrochem. Soc.* **1979**, *126*
5
6 (12), 2047–2051.
7
- 8
9 (4) Peled, E.; Golodnitsky, D.; Penciner, J. The Anode/Electrolyte Interface. *Handb. Batter.*
10
11 *Mater. Second Ed.* **2011**, No. until 1982, 479–523.
12
- 13 (5) Peled, E.; Menkin, S. Review-SEI: Past, Present and Future. *J. Electrochem. Soc.* **2017**, *164*
14
15 (7), A1703–A1719.
16
- 17 (6) Wang, A.; Kadam, S.; Li, H.; Shi, S.; Qi, Y. Review on Modeling of the Anode Solid
18
19 Electrolyte Interphase (SEI) for Lithium-Ion Batteries. *npj Comput. Mater* **2018**, *4*, 1–15.
20
- 21 (7) An, S. J.; Li, J.; Daniel, C.; Mohanty, D.; Nagpure, S.; Wood, D. L. The State of
22
23 Understanding of the Lithium-Ion-Battery Graphite Solid Electrolyte Interphase (SEI) and
24
25 Its Relationship to Formation Cycling. *Carbon N. Y.* **2016**, *105*, 52–76.
26
- 27 (8) Obrovac, M. N.; Chevrier, V. L. Alloy Negative Electrodes for Li-Ion Batteries. *Chem. Rev.*
28
29 **2014**, *114* (23), 11444–11502.
30
- 31 (9) Obrovac, M. N.; Christensen, L.; Le, D. B.; Dahn, J. R. Alloy Design for Lithium-Ion
32
33 Battery Anodes. *J. Electrochem. Soc.* **2007**, *154* (9), A849–A855.
34
- 35 (10) Wu, H.; Cui, Y. Designing Nanostructured Si Anodes for High Energy Lithium Ion
36
37 Batteries. *Nano Today* **2012**, *7* (5), 414–429.
38
- 39 (11) Andre, D.; Hain, H.; Lamp, P.; Maglia, F.; Stiaszny, B. Future High-Energy Density Anode
40
41 Materials from an Automotive Application Perspective. *J. Mater. Chem. A* **2017**, *5* (33),
42
43 17174–17198.
44
- 45 (12) Du, Z.; Li, J.; Daniel, C.; Wood, D. L. Si Alloy/Graphite Coating Design as Anode for Li-
46
47 Ion Batteries with High Volumetric Energy Density. *Electrochim. Acta* **2017**, *254*, 123–
48
49
50
51
52
53
54
55
56
57
58
59
60

- 1
2
3 129.
4
5
6 (13) Chae, S.; Ko, M.; Kim, K.; Ahn, K.; Cho, J. Confronting Issues of the Practical
7 Implementation of Si Anode in High-Energy Lithium-Ion Batteries. *Joule* **2017**, *1* (1), 47–
8 60.
9
10
11
12 (14) Choi, J. W.; Aurbach, D. Promise and Reality of Post-Lithium-Ion Batteries with High
13 Energy Densities. *Nat. Rev. Mater.* **2016**, *1*, 16013.
14
15
16 (15) Obrovac, M. N.; Christensen, L. Structural Changes in Silicon Anodes during Lithium
17 Insertion/Extraction. *Electrochem. Solid-State Lett.* **2004**, *7* (5), A93–A96.
18
19
20
21 (16) Son, I. H.; Park, J. H.; Kwon, S.; Park, S.; Rummeli, M. H.; Bachmatiuk, A.; Song, H. J.;
22 Ku, J.; Choi, J. W.; Choi, J. M.; Doo S.-G.; Chang H.; Silicon Carbide-Free Graphene
23 Growth on Silicon for Lithium-Ion Battery with High Volumetric Energy Density. *Nat.*
24 *Commun.* **2015**, *6*, 7393.
25
26
27
28
29 (17) Wang, C.; Wu, H.; Chen, Z.; McDowell, M. T.; Cui, Y.; Bao, Z. Self-Healing Chemistry
30 Enables the Stable Operation of Silicon Microparticle Anodes for High-Energy Lithium-
31 Ion Batteries. *Nat. Chem.* **2013**, *5* (12), 1042–1048.
32
33
34
35 (18) Wu, H.; Yu, G.; Pan, L.; Liu, N.; McDowell, M. T.; Bao, Z.; Cui, Y. Stable Li-Ion Battery
36 Anodes by in-Situ Polymerization of Conducting Hydrogel to Conformally Coat Silicon
37 Nanoparticles. *Nat. Commun.* **2013**, *4*, 1943–1946.
38
39
40
41 (19) Li, J.; Lewis, R. B.; Dahn, J. R. Sodium Carboxymethyl Cellulose A Potential Binder for Si
42 Negative Electrodes for Li-Ion Batteries. *Electrochem. Solid-State Lett.* **2007**, *10* (2), A17–
43 A20.
44
45
46
47 (20) Michan, A. L.; Divitini, G.; Pell, A. J.; Leskes, M.; Ducati, C.; Grey, C. P. Solid Electrolyte
48 Interphase Growth and Capacity Loss in Silicon Electrodes. *J. Am. Chem. Soc.* **2016**, *138*
49
50
51
52
53
54
55
56
57
58
59
60

- (25), 7918–7931.
- (21) Wu, H.; Chan, G.; Choi, J. W.; Ryu, I.; Yao, Y.; Mcdowell, M. T.; Lee, S. W.; Jackson, A.; Yang, Y.; Hu, L.; Cui, Y. Stable Cycling of Double-Walled Silicon Nanotube Battery Anodes through Solid-Electrolyte Interphase Control. *Nat. Nanotechnol.* **2012**, *7* (5), 310–315.
- (22) Yang, J.; Solomatin, N.; Kraysberg, A.; Ein-Eli, Y. In-Situ Spectro-Electrochemical Insight Revealing Distinctive Silicon Anode Solid Electrolyte Interphase Formation in a Lithium-Ion Battery. *ChemistrySelect* **2016**, *1* (3), 572–576.
- (23) Schroder, K. W.; Celio, H.; Webb, L. J.; Stevenson, K. J. Examining Solid Electrolyte Interphase Formation on Crystalline Silicon Electrodes: Influence of Electrochemical Preparation and Ambient Exposure Conditions. *J. Phys. Chem. C* **2012**, *116* (37), 19737–19747.
- (24) Veith, G. M.; Doucet, M.; Sacci, R. L.; Vacaliuc, B.; Baldwin, J. K.; Browning, J. F. Determination of the Solid Electrolyte Interphase Structure Grown on a Silicon Electrode Using a Fluoroethylene Carbonate Additive. *Sci. Rep.* **2017**, *7* (1), 1–15.
- (25) Philippe, B.; Dedryvère, R.; Allouche, J.; Lindgren, F.; Gorgoi, M.; Rensmo, H.; Gonbeau, D.; Edström, K. Nanosilicon Electrodes for Lithium-Ion Batteries: Interfacial Mechanisms Studied by Hard and Soft X-Ray Photoelectron Spectroscopy. *Chem. Mater.* **2012**, *24* (6), 1107–1115.
- (26) Shi, F.; Ross, P. N.; Somorjai, G. A.; Komvopoulos, K. The Chemistry of Electrolyte Reduction on Silicon Electrodes Revealed by in Situ ATR-FTIR Spectroscopy. *J. Phys. Chem. C* **2017**, *121* (27), 14476–14483.
- (27) Jin, Y.; Zhu, B.; Lu, Z.; Liu, N.; Zhu, J. Challenges and Recent Progress in the Development

- 1
2
3 of Si Anodes for Lithium-Ion Battery. *Adv. Energy Mater.* **2017**, 1700715.
- 4
5 (28) Ozanam, F.; Rosso, M. Silicon as Anode Material for Li-Ion Batteries. *Mater. Sci. Eng. B*
6
7 *Solid-State Mater. Adv. Technol.* **2016**, 213, 2–11.
- 8
9
10 (29) Veith, G. M.; Doucet, M.; Baldwin, J. K.; Sacci, R. L.; Fears, T. M.; Wang, Y.; Browning,
11
12 J. F. Direct Determination of Solid-Electrolyte Interphase Thickness and Composition as a
13
14 Function of State of Charge on a Silicon Anode. *J. Phys. Chem. C* **2015**, 119 (35), 20339–
15
16 20349.
- 17
18
19 (30) Xu, K. Nonaqueous Liquid Electrolytes for Lithium-Based Rechargeable Batteries. **2004**,
20
21 *104*, 4303–4418.
- 22
23
24 (31) Steinrück, H. G.; Cao, C.; Veith, G. M.; Toney, M. F. Toward Quantifying Capacity Losses
25
26 Due to Solid Electrolyte Interphase Evolution in Silicon Thin Film Batteries. *J. Chem. Phys.*
27
28 **2020**, 152 (8).
- 29
30
31 (32) Ross, P. N. Catalysis and Interfacial Chemistry in Lithium Batteries: A Surface Science
32
33 Approach. *Catal. Letters* **2014**, 144 (8), 1370–1376.
- 34
35
36 (33) Shi, F.; Ross, P. N.; Zhao, H.; Liu, G.; Somorjai, G. A.; Komvopoulos, K. A Catalytic Path
37
38 for Electrolyte Reduction in Lithium-Ion Cells Revealed by in Situ Attenuated Total
39
40 Reflection-Fourier Transform Infrared Spectroscopy. *J. Am. Chem. Soc.* **2015**, 137 (9),
41
42 3181–3184.
- 43
44
45 (34) Li, J.; Dozier, A. K.; Li, Y.; Yang, F.; Cheng, Y.-T. Crack Pattern Formation in Thin Film
46
47 Lithium-Ion Battery Electrodes. *J. Electrochem. Soc.* **2011**, 158 (6), A689.
- 48
49
50 (35) Schroder, K. W.; Dylla, A. G.; Harris, S. J.; Webb, L. J.; Stevenson, K. J. Role of Surface
51
52 Oxides in the Formation of Solid-Electrolyte Interphases at Silicon Electrodes for Lithium-
53
54 Ion Batteries. *ACS Appl. Mater. Interfaces* **2014**, 6 (23), 21510–21524.
- 55
56
57
58
59
60

- 1
2
3 (36) Abel, P. R.; Lin, Y. M.; Celio, H.; Heller, A.; Mullins, C. B. Improving the Stability of
4 Nanostructured Silicon Thin Film Lithium-Ion Battery Anodes through Their Controlled
5 Oxidation. *ACS Nano* **2012**, *6* (3), 2506–2516.
6
7
8
9
10 (37) Schroder, K. W.; Dylla, A. G.; Harris, S. J.; Webb, L. J.; Stevenson, K. J. Role of Surface
11 Oxides in the Formation of Solid – Electrolyte Interphases at Silicon Electrodes for
12 Lithium-Ion Batteries. **2014**.
13
14
15
16
17 (38) Ferraresi, G.; Czornomaz, L.; Villeveille, C.; Novák, P.; El Kazzi, M. Elucidating the
18 Surface Reactions of an Amorphous Si Thin Film as a Model Electrode for Li-Ion Batteries.
19 *ACS Appl. Mater. Interfaces* **2016**, *8* (43), 29791–29798.
20
21
22
23
24 (39) Tübke, J.; Pinkwart, K.; Hendricks, C. E.; Fuentevilla, D. A.; Doering, H.; Liebau, V.; Feng,
25 X.; Ouyang, M.; Lu, L.; Hollmotz, L.; Vogt, J. *Li-Secondary Battery*; Garche, J., Brandt,
26 K., Eds.; Elsevier B.V, 2018.
27
28
29
30
31 (40) Zhuang, G. V.; Xu, K.; Yang, H.; Jow, T. R.; Ross, P. N. Lithium Ethylene Dicarboxylate
32 Identified as the Primary Product of Chemical and Electrochemical Reduction of EC in 1.2
33 M LiPF₆/EC:EMC Electrolyte. *J. Phys. Chem. B* **2005**, *109* (37), 17567–17573.
34
35
36
37
38 (41) Xu, K.; Zhuang, G. V.; Allen, J. L.; Lee, U.; Zhang, S. S.; Ross, P. N.; Jow, T. R. Syntheses
39 and Characterization of Lithium Alkyl Mono- and Bicarbonates as Components of Surface
40 Films in Li-Ion Batteries. *J. Phys. Chem. B* **2006**, *110* (15), 7708–7719.
41
42
43
44
45 (42) Nie, M.; Lucht, B. L. Role of Lithium Salt on Solid Electrolyte Interface (SEI) Formation
46 and Structure in Lithium Ion Batteries. *J. Electrochem. Soc.* **2014**, *161* (6), A1001–A1006.
47
48
49
50 (43) Nie, M.; Abraham, D. P.; Chen, Y.; Bose, A.; Lucht, B. L. Silicon Solid Electrolyte
51 Interphase (SEI) of Lithium Ion Battery Characterized by Microscopy and Spectroscopy. *J.*
52 *Phys. Chem. C* **2013**, *117*, 13403–13412.
53
54
55
56
57
58
59
60

- 1
2
3 (44) Parimalam, B. S.; MacIntosh, A. D.; Kadam, R.; Lucht, B. L. Decomposition Reactions of
4 Anode Solid Electrolyte Interphase (SEI) Components with LiPF₆. *J. Phys. Chem. C* **2017**,
5 *121* (41), 22733–22738.
6
7
8
9
10 (45) Aurbach, D. A Comparative Study of Synthetic Graphite and Li Electrodes in Electrolyte
11 Solutions Based on Ethylene Carbonate-Dimethyl Carbonate Mixtures. *J. Electrochem.*
12 *Soc.* **1996**, *143* (12), 3809–3820.
13
14
15
16
17 (46) Aurbach, D.; Gofer, Y.; Ben-Zion, M.; Aped, P. The Behaviour of Lithium Electrodes in
18 Propylene and Ethylene Carbonate: The Major Factors That Influence Li Cycling
19 Efficiency. *J. Electroanal. Chem.* **1992**, *339* (1–2), 451–471.
20
21
22
23
24 (47) Aurbach, D. The Surface Chemistry of Lithium Electrodes in Alkyl Carbonate Solutions. *J.*
25 *Electrochem. Soc.* **1994**, *141* (1), L1–L3.
26
27
28
29 (48) Zhuang, G. V.; Yang, H.; Blizanac, B.; Ross, P. N. A Study of Electrochemical Reduction
30 of Ethylene and Propylene Carbonate Electrolytes on Graphite Using ATR-FTIR
31 Spectroscopy. *Electrochem. Solid-State Lett.* **2005**, *8* (9), A441–A445.
32
33
34
35 (49) Ariel, N.; Ceder, G.; Sadoway, D. R.; Fitzgerald, E. A. Electrochemically Controlled
36 Transport of Lithium through Ultrathin SiO₂. *J. Appl. Phys.* **2005**, *98* (2).
37
38
39
40 (50) Sivonxay, E.; Aykol, M.; Persson, K. A. The Lithiation Process and Li Diffusion in
41 Amorphous SiO₂ and Si from First-Principles. *Electrochim. Acta* **2020**, *331*, 135344.
42
43
44
45 (51) Tasaki, K.; Harris, S. J. Computational Study on the Solubility of Lithium Salts Formed on
46 Lithium Ion Battery Negative Electrode in Organic Solvents. *J. Phys. Chem. C* **2010**, *114*
47 (17), 8076–8083.
48
49
50
51 (52) Tasaki, K.; Goldberg, A.; Lian, J.-J.; Walker, M.; Timmons, A.; Harris, S. J. Solubility of
52 Lithium Salts Formed on the Lithium-Ion Battery Negative Electrode Surface in Organic
53
54
55
56
57
58
59
60

- 1
2
3 Solvents. *J. Electrochem. Soc.* **2009**, *156* (12), A1019–A1019.
- 4
5 (53) Jin, Y.; Kneusels, N. J. H.; Magusin, P. C. M. M.; Kim, G.; Castillo-Martínez, E.; Marbella,
6 L. E.; Kerber, R. N.; Howe, D. J.; Paul, S.; Liu, T.; Grey, C.P. Identifying the Structural
7 Basis for the Increased Stability of the Solid Electrolyte Interphase Formed on Silicon with
8 the Additive Fluoroethylene Carbonate. *J. Am. Chem. Soc.* **2017**, *139* (42), 14992–15004..
9
10
11
12
13
14 (54) Nanda, J.; Yang, G.; Hou, T.; Voylov, D. N.; Li, X.; Ruther, R. E.; Naguib, M.; Persson,
15 K.; Veith, G. M.; Sokolov, A. P. Unraveling the Nanoscale Heterogeneity of Solid
16 Electrolyte Interphase Using Tip-Enhanced Raman Spectroscopy. *Joule* **2019**, *3* (8), 2001–
17 2019.
18
19
20
21
22
23 (55) Keilmann, F.; Hillenbrand, R. Near-Field Microscopy by Elastic Light Scattering from a
24 Tip. *Philos. Trans. R. Soc. A Math. Phys. Eng. Sci.* **2004**, *362* (1817), 787–805.
25
26
27 (56) McLeod, A. S.; Kelly, P.; Goldflam, M. D.; Gainsforth, Z.; Westphal, A. J.; Dominguez,
28 G.; Thiemens, M. H.; Fogler, M. M.; Basov, D. N. Model for Quantitative Tip-Enhanced
29 Spectroscopy and the Extraction of Nanoscale-Resolved Optical Constants. *Phys. Rev. B -*
30 *Condens. Matter Mater. Phys.* **2014**, *90* (8), 1–17.
31
32
33 (57) Ayache, M.; Lux, S. F.; Kostecki, R. IR Near-Field Study of the Solid Electrolyte Interphase
34 on a Tin Electrode. *J. Phys. Chem. Lett.* **2015**, *6* (7), 1126–1129.
35
36
37 (58) Ayache, M.; Jang, D.; Syzdek, J.; Kostecki, R. Near-Field IR Nanoscale Imaging of the
38 Solid Electrolyte Interphase on a HOPG Electrode. *J. Electrochem. Soc.* **2015**, *162* (13),
39 A7078–A7082.
40
41
42 (59) Song, S. W.; Baek, S. W. Surface Layer Formation on Sn Anode: ATR FTIR Spectroscopic
43 Characterization. *Electrochim. Acta* **2009**, *54* (4), 1312–1318.
44
45
46 (60) Plakhotnyk, A. V; Ernst, L.; Schmutzler, R. Hydrolysis in the System LiPF₆ - Propylene
47
48
49
50
51
52
53
54
55
56
57
58
59
60

- 1
2
3 Carbonate - Dimethyl Carbonate - H₂O. *J. Fluor. Chem.* **2005**, *126* (1), 27–31.
- 4
5
6 (61) Terborg, L.; Nowak, S.; Passerini, S.; Winter, M.; Karst, U.; Haddad, P. R.; Nesterenko, P.
7
8 N. Ion Chromatographic Determination of Hydrolysis Products of Hexafluorophosphate
9
10 Salts in Aqueous Solution. *Anal. Chim. Acta* **2012**, *714*, 121–126.
- 11
12 (62) Solchenbach, S.; Metzger, M.; Egawa, M.; Beyer, H.; Gasteiger, H. A. Quantification of
13
14 PF₅ and POF₃ from Side Reactions of LiPF₆ in Li-Ion Batteries. *J. Electrochem. Soc.* **2018**,
15
16 *165* (13), A3022–A3028.
- 17
18 (63) Philippe, B.; Dedryvère, R.; Gorgoi, M.; Rensmo, H.; Gonbeau, D.; Edström, K. Role of
19
20 the LiPF₆ Salt for the Long-Term Stability of Silicon Electrodes in Li-Ion Batteries - A
21
22 Photoelectron Spectroscopy Study. *Chem. Mater.* **2013**, *25* (3), 394–404.
- 23
24 (64) Lux, S. F.; Lucas, I. T.; Pollak, E.; Passerini, S.; Winter, M.; Kostecki, R. The Mechanism
25
26 of HF Formation in LiPF₆ Based Organic Carbonate Electrolytes. *Electrochem. commun.*
27
28 **2012**, *14* (1), 47–50.
- 29
30 (65) Mitra, A.; Rimstidt, J. D. Solubility and Dissolution Rate of Silica in Acid Fluoride
31
32 Solutions. *Geochim. Cosmochim. Acta* **2009**, *73* (23), 7045–7059.
- 33
34 (66) Lee, J. H.; Hwangbo, C. K. U. Inhomogeneous Refractive Index of SiO_xF_y Thin Films
35
36 Prepared by Ion Beam Assisted Deposition. *Surf. Coatings Technol.* **2000**, *128–129*, 280–
37
38 285.
- 39
40 (67) DuMont, J. W.; Marquardt, A. E.; Cano, A. M.; George, S. M. Thermal Atomic Layer
41
42 Etching of SiO₂ by a “Conversion-Etch” Mechanism Using Sequential Reactions of
43
44 Trimethylaluminum and Hydrogen Fluoride. *ACS Appl. Mater. Interfaces* **2017**, *9* (11),
45
46 10296–10307.
- 47
48 (68) El Ouatani, L.; Dedryvère, R.; Siret, C.; Biensan, P.; Reynaud, S.; Iratçabal, P.; Gonbeau,
49
50
51
52
53
54
55
56
57
58
59
60

- 1
2
3 D. The Effect of Vinylene Carbonate Additive on Surface Film Formation on Both
4 Electrodes in Li-Ion Batteries. *J. Electrochem. Soc.* **2009**, *156* (2), A103–A113.
5
6
7
8 (69) Bi, Y.; Wang, T.; Liu, M.; Du, R.; Yang, W.; Liu, Z.; Peng, Z.; Liu, Y.; Wang, D.; Sun, X.
9
10 Stability of Li₂CO₃ in Cathode of Lithium Ion Battery and Its Influence on Electrochemical
11 Performance. *RSC Adv.* **2016**, *6* (23), 19233–19237.
12
13
14 (70) Wotango, A. S.; Su, W. N.; Leggesse, E. G.; Haregewoin, A. M.; Lin, M. H.; Zegeye, T.
15 A.; Cheng, J. H.; Hwang, B. J. Improved Interfacial Properties of MCMB Electrode by 1-
16 (Trimethylsilyl)Imidazole as New Electrolyte Additive to Suppress LiPF₆ Decomposition.
17 *ACS Appl. Mater. Interfaces* **2017**, *9* (3), 2410–2420.
18
19
20 (71) Kawamura, T.; Okada, S.; Yamaki, J. ichi. Decomposition Reaction of LiPF₆-Based
21 Electrolytes for Lithium Ion Cells. *J. Power Sources* **2006**, *156* (2), 547–554.
22
23
24 (72) Qiao, R.; Lucas, I. T.; Karim, A.; Syzdek, J.; Liu, X.; Chen, W.; Persson, K.; Kostecki, R.;
25 Yang, W. Distinct Solid-Electrolyte-Interphases on Sn (100) and (001) Electrodes Studied
26 by Soft X-Ray Spectroscopy. *Adv. Mater. Interfaces* **2014**, *1* (3), 1–6.
27
28
29 (73) Li, C.; Gu, L.; Maier, J. Enhancement of the Li Conductivity in LiF by Introducing
30 Glass/Crystal Interfaces. *Adv. Funct. Mater.* **2012**, *22* (6), 1145–1149.
31
32
33 (74) Zhuo, Z.; Lu, P.; Delacourt, C.; Qiao, R.; Xu, K.; Pan, F.; Harris, S. J.; Yang, W. Breathing
34 and Oscillating Growth of Solid-Electrolyte-Interphase upon Electrochemical Cycling.
35 *Chem. Commun.* **2018**, *54*, 814–817.
36
37
38 (75) Wu, W.; Nancollas, G. H. The Dissolution and Growth of Sparingly Soluble Inorganic Salts:
39 A Kinetics and Surface Energy Approach. *Pure Appl. Chem.* **1998**, *70* (10), 1867–1872.
40
41
42 (76) Smith, B. T. Solubility and Dissolution. In *Remington Education: Physical Pharmacy*;
43 Pharmaceutical Press, Ed.; 2015.
44
45
46
47
48
49
50
51
52
53
54
55
56
57
58
59
60

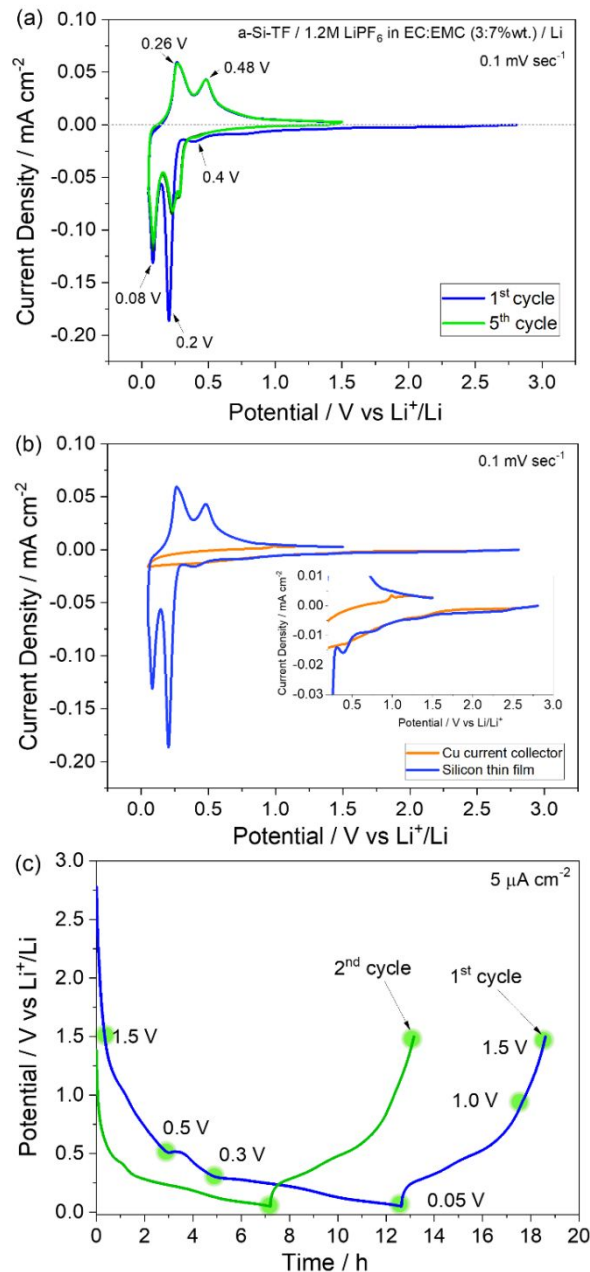


Figure 1. (a) Cyclic voltammetry of 50 nm a-Si-TF electrodes in Gen 2 electrolyte (1.2 M LiPF₆ in EC:EMC 3:7 wt.%). (b) Comparison of the 1st cycle voltammetric profile of the a-Si-TF and the bare copper current collector. (c) 1st and 2nd galvanostatic cycle of a-Si-TF cycled at 5 μA cm⁻² within the 0.05 V-1.5 V vs Li⁺/Li potential range. Green dots represent the potentials at which *ex situ* surface analysis of a-Si-TF electrodes has been performed.

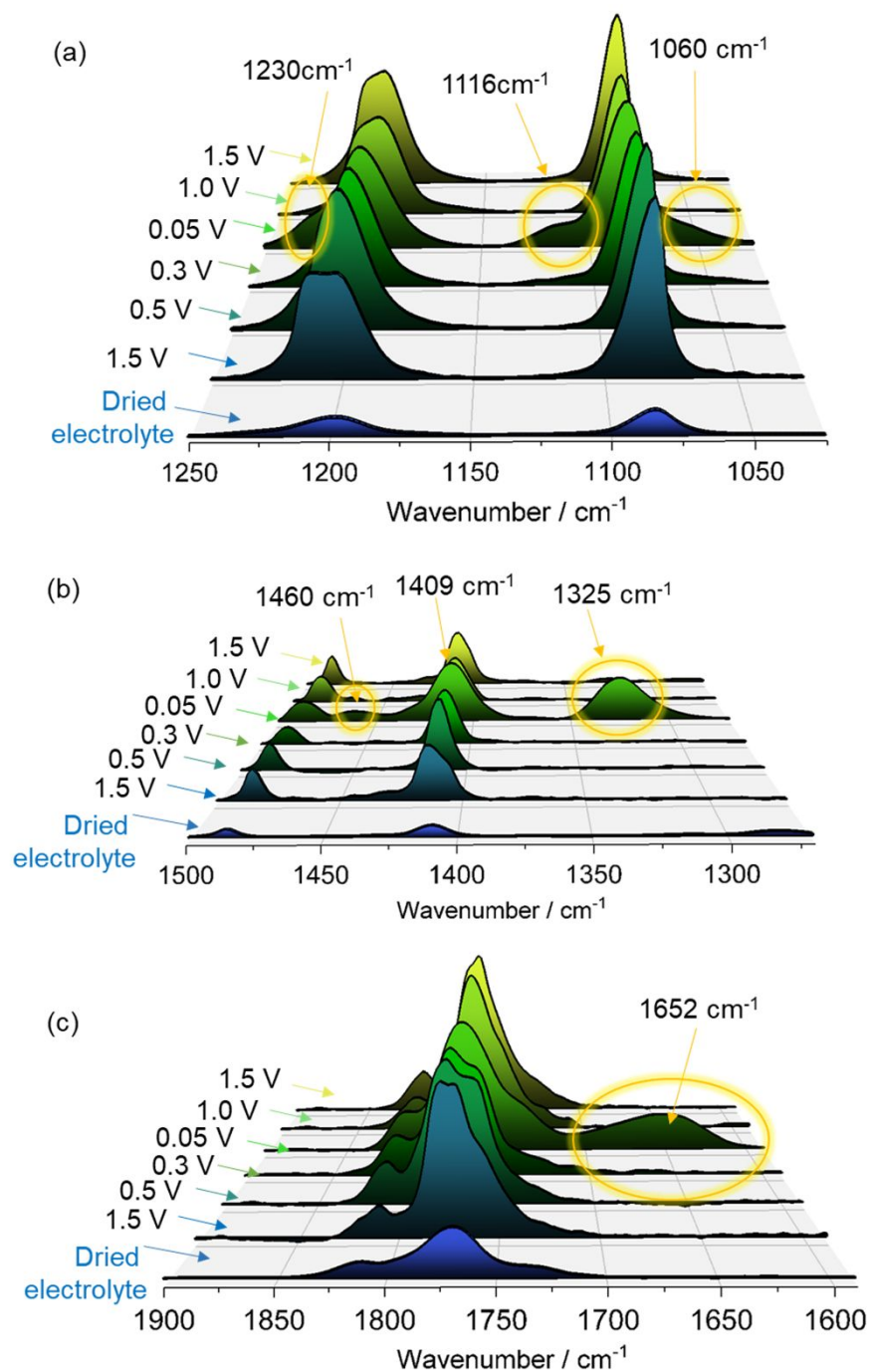
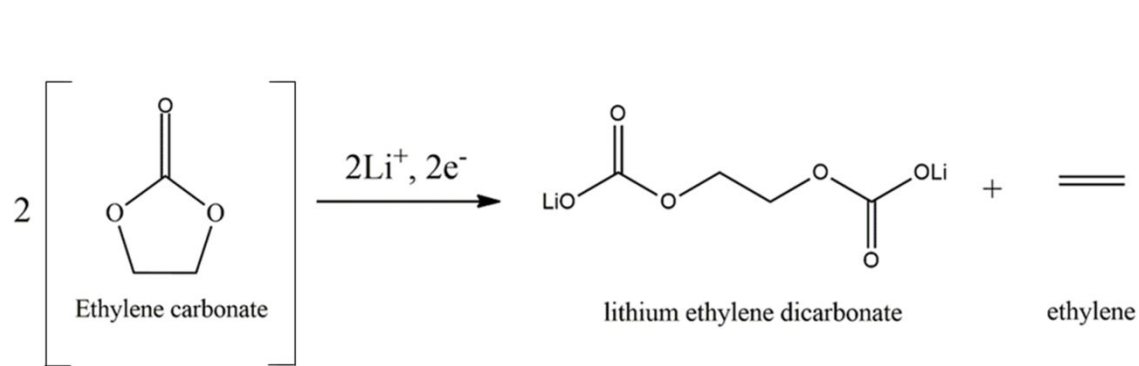


Figure 2. (a-c) Selected spectral regions of *ex situ* ATR-FTIR spectra of cycled a-Si-TFs at various potentials during the first lithiation/de-lithiation process. The electrodes have not been washed prior analysis.



13 **Scheme 1.** Single electron reduction of EC leading to the formation of LiEDC and ethylene.⁴⁰

14 Reprinted in part and adapted from ref. ⁴⁰. Copyright 2005 American Chemical Society.

15
16
17
18
19
20
21
22
23
24
25
26
27
28
29
30
31
32
33
34
35
36
37
38
39
40
41
42
43
44
45
46
47
48
49
50
51
52
53
54
55
56
57
58
59
60

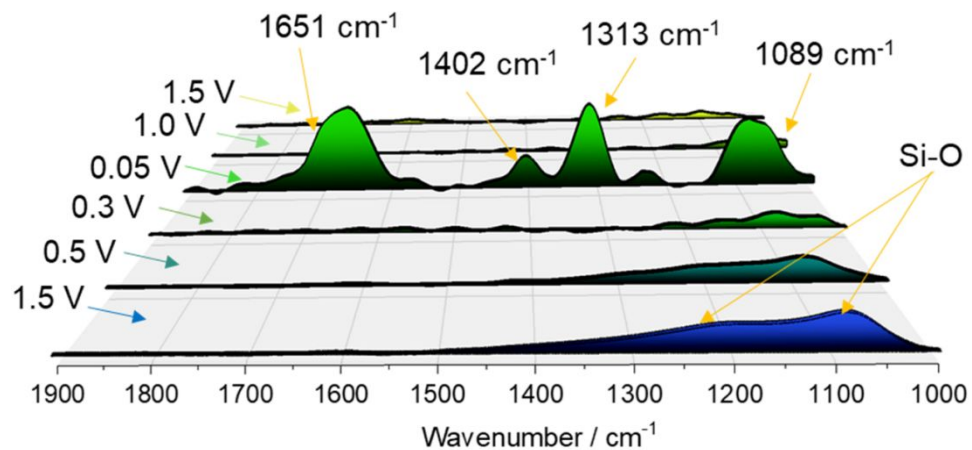
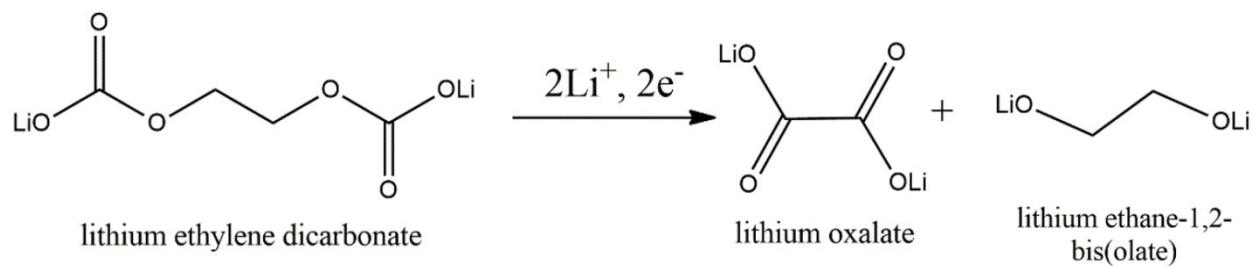


Figure 3. *Ex situ* ATR-FTIR analysis of cycled a-Si-TF electrode at different potentials during the first lithiation/de-lithiation process. The electrodes have been washed in DEC for 10s prior to analysis.



14 **Scheme 2.** Two electron reduction process of LiEDC leading to the formation of lithium oxalate
15 and lithium ethane-1,2-bis(olate). Reprinted in part and adapted from ref. ⁴⁸ Copyright 2005 The
16
17
18 Electrochemical Society.
19
20
21
22
23
24
25
26
27
28
29
30
31
32
33
34
35
36
37
38
39
40
41
42
43
44
45
46
47
48
49
50
51
52
53
54
55
56
57
58
59
60

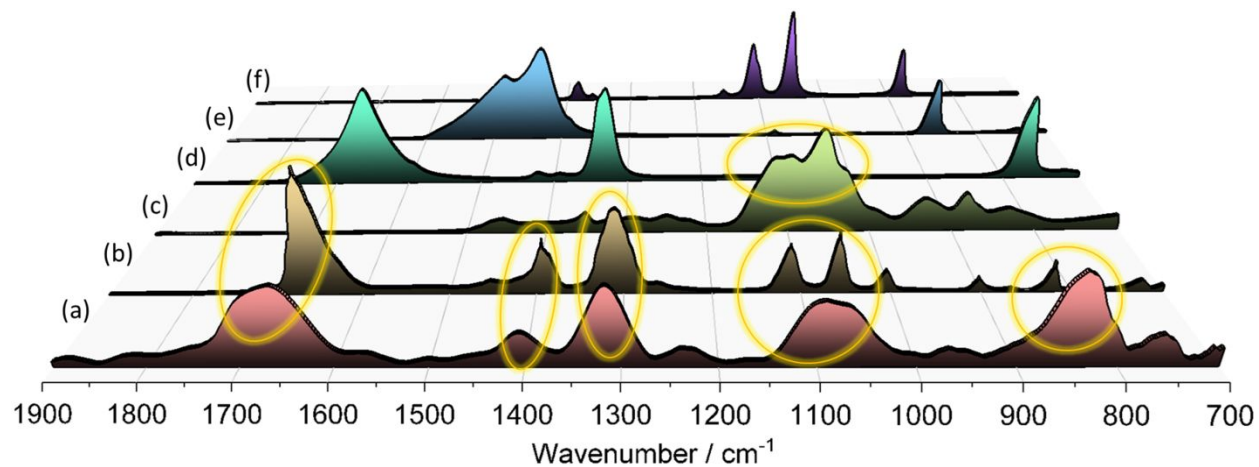
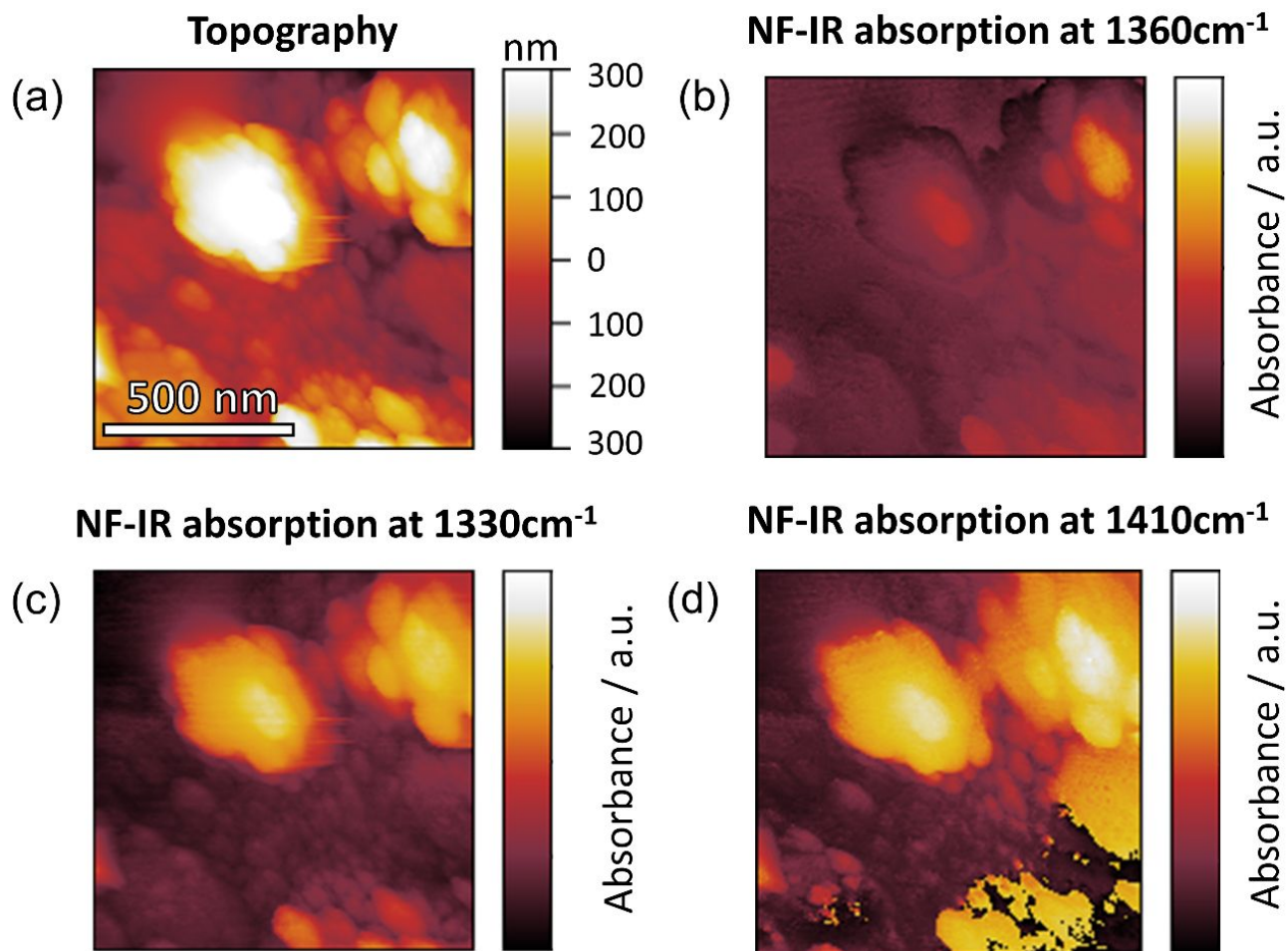


Figure 4. ATR-FTIR spectrum of (a) lithiated (0.05 V) washed a-Si-TF electrode compared with reference spectrum of (b) lithium ethylene decarbonate (LiEDC),⁴⁰ (c) polyethylene glycol (PEG), (d) lithium oxalate, (e) lithium carbonate and (f) lithium ethoxide. The spectrum of LiEDC has been reprinted and adapted with permission from ref ⁴⁰ Copyright 2005 American Chemical Society.



36 **Figure 5.** *Ex situ* IR aNSOM 1 x 1 μm images of the lithiated a-Si-TF electrode at 0.05 V; (a) AFM
37 topography, and corresponding near-field IR absorption images at (b) 1360 cm⁻¹, (c) 1330 cm⁻¹,
38 and (d) 1410 cm⁻¹.
39
40
41
42
43
44
45
46
47
48
49
50
51
52
53
54
55
56
57
58
59
60

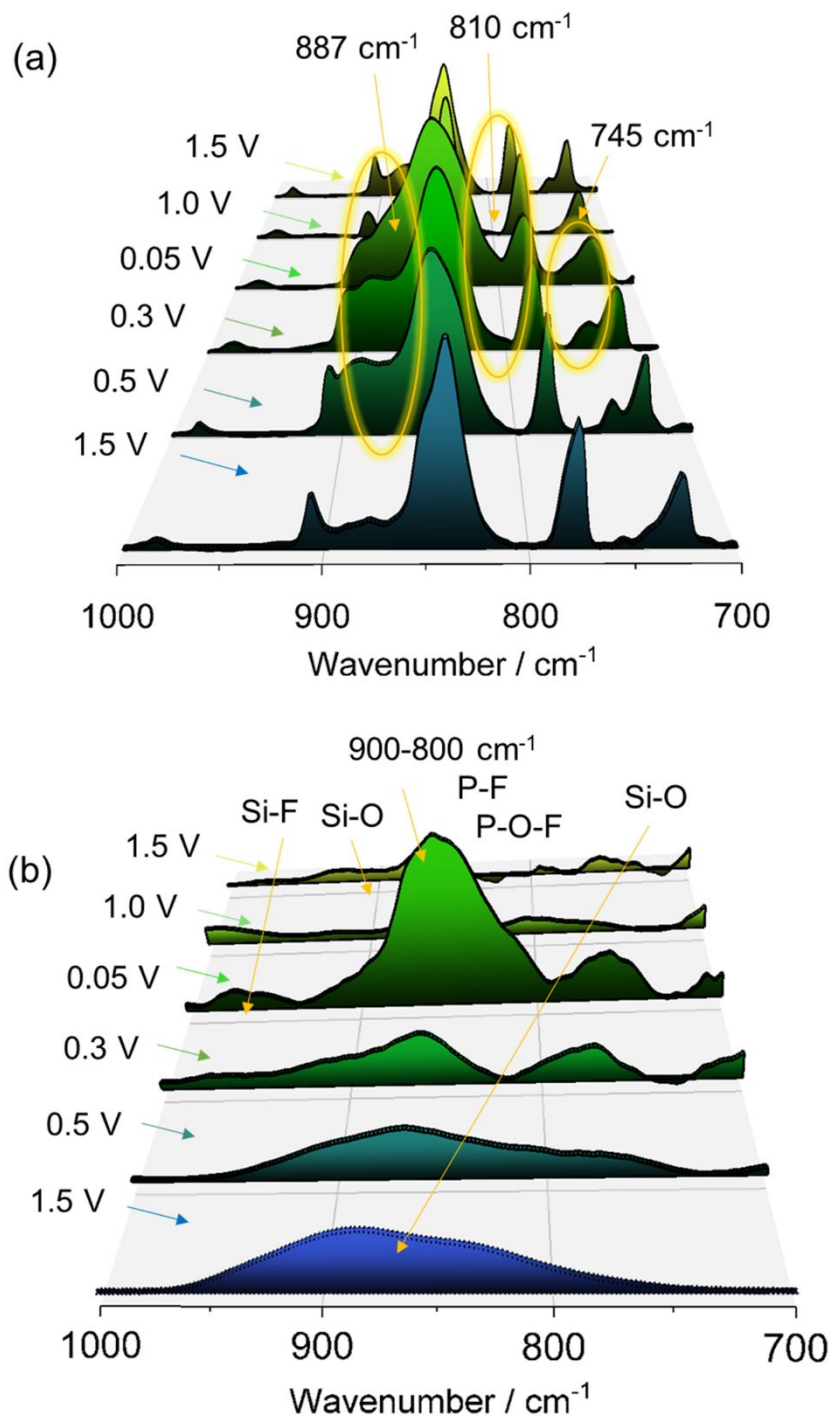
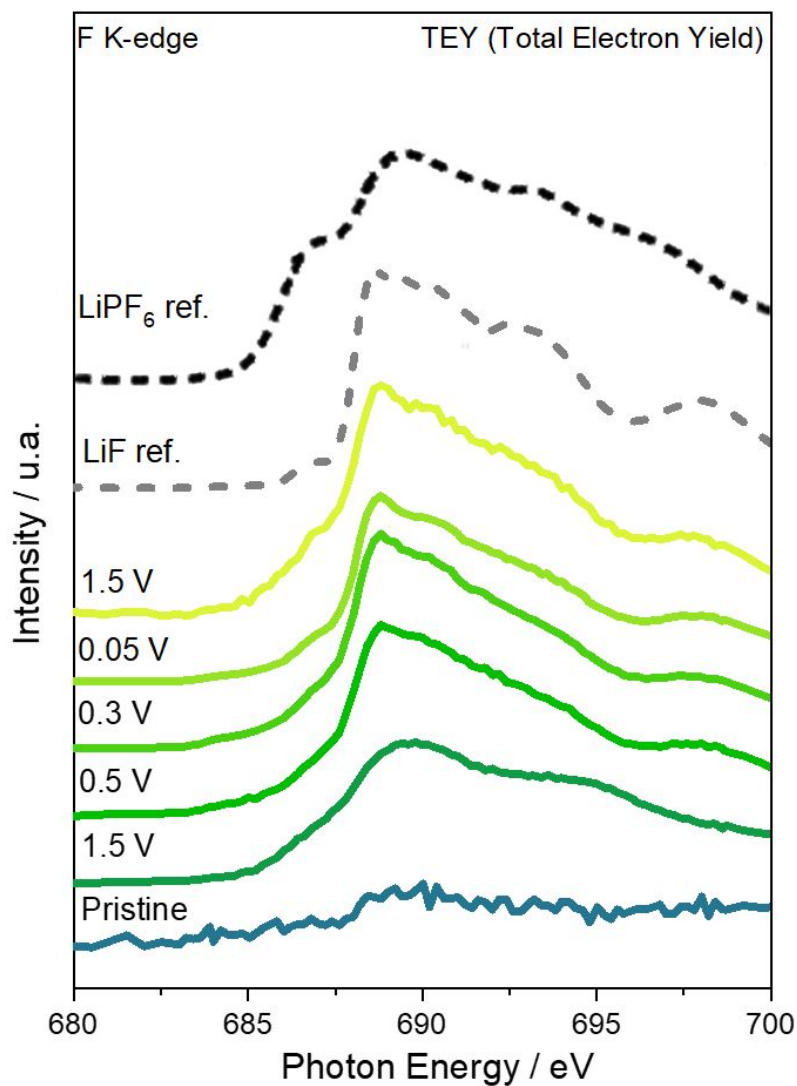


Figure 6. *Ex situ* ATR-FTIR analysis of not washed (a) and washed (b) cycled a-Si-TF electrodes at different potentials during the first lithiation/de-lithiation process.



41 **Figure 7.** *Ex situ* F K-edge XAS TEY spectra of the SEI layer formed during the 1st cycle on the
42 a-Si-TF electrodes (washed) at different potentials. The LiF and LiPF₆ spectra are shown as
43 reference.
44
45
46
47
48
49
50
51
52
53
54
55
56
57
58
59
60

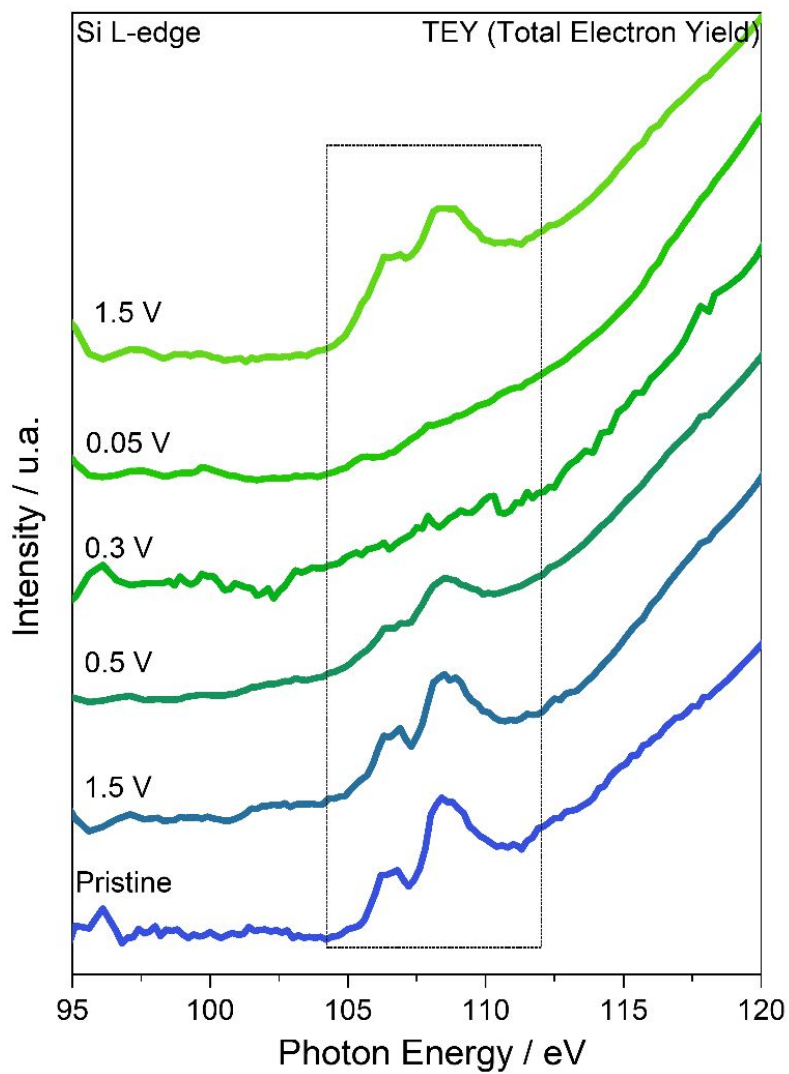


Figure 8. Si L-edge XAS TEY spectra of the SEI layer formed on the a-Si-TF electrodes during the 1st cycle at different potentials. Electrodes were washed in DEC prior to XAS measurements.

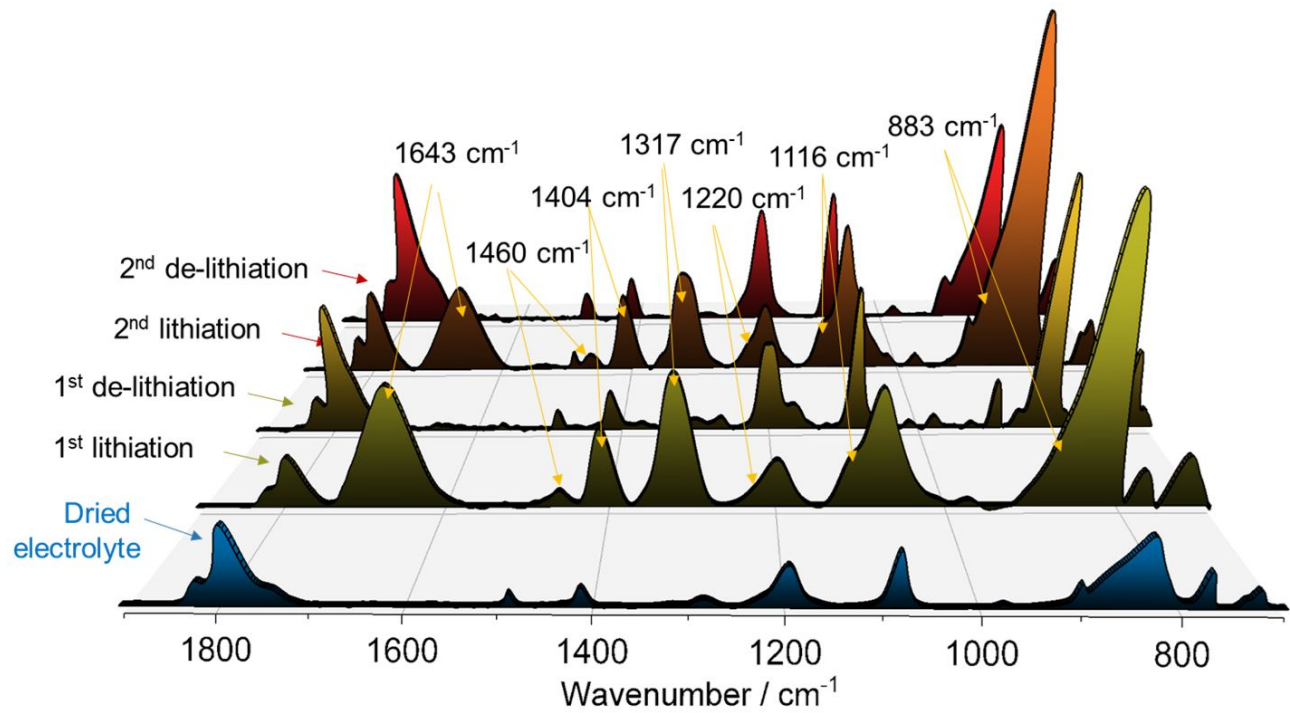


Figure 9. *Ex situ* ATR-FTIR spectra of the a-Si-TF electrodes at 0.05 and 1.5 V during 1st and 2nd galvanostatic cycles. The electrodes have not been washed in DEC prior analysis.

For Table of Contents Only

